

Luminescent Properties of Pure Cubic Phase $\text{Y}_2\text{O}_3/\text{Eu}^{3+}$ Nanotubes/Nanowires Prepared by a Hydrothermal Method

Xue Bai,^{†,‡} Hongwei Song,^{*,†} Lixin Yu,^{†,‡} Linmei Yang,^{†,‡} Zhongxin Liu,^{†,‡} Guohui Pan,^{†,‡} Shaozhe Lu,[†] Xingguang Ren,[†] Yanqiang Lei,^{†,‡} and Libo Fan^{†,‡}

Key Laboratory of Excited State Physics, Changchun Institute of Optics, Fine Mechanics and Physics, Chinese Academy of Sciences, 16 Eastern Nan-Hu Road, Changchun 130033, P.R. China, and Graduate School of Chinese Academy of Sciences, 16 Eastern Nan-Hu Road, Changchun 130033, P.R. China

Received: February 6, 2005; In Final Form: May 25, 2005

One-dimensional pure cubic $\text{Y}_2\text{O}_3/\text{Eu}^{3+}$ nanocrystals (NCs) were synthesized by a hydrothermal method at various temperatures. The NCs prepared at 130 °C yielded nanotubes (NTs) with wall thickness of 5–10 nm and outer diameter of 20–40 nm. The NCs prepared at 170 and 180 °C yielded nanowires (NWs) with diameters of ~100 and ~300 nm, respectively. Their luminescent properties, including electronic transition processes, local environments surrounding Eu^{3+} ions, electron–phonon coupling, and UV light irradiation induced spectral changes have been systematically studied and compared. The results indicate that the $\text{Y}_2\text{O}_3/\text{Eu}^{3+}$ NTs and NWs have strong red $^5\text{D}_0$ – $^7\text{F}_2$ transitions. The fluorescence lifetime of $^5\text{D}_1$ – $^7\text{F}_1$ hardly changes in different samples, while that of $^5\text{D}_0$ – $^7\text{F}_2$ decreases a small amount in $\text{Y}_2\text{O}_3/\text{Eu}^{3+}$ NTs. The $^5\text{D}_0$ – $^7\text{F}_2$ lines originate from the emissions of Eu^{3+} ions occupying one C_2 site, like that in the bulk powders. The phonon sideline with a frequency shift of 40–50 cm^{-1} appears at the low-energy side of the $^7\text{F}_0$ – $^5\text{D}_0$ zero phonon line. The relative intensity of the sideline to zero phonon line increases by varying from NTs to NWs, and the spectral position of the phonon sideline shifts red. The UV light irradiation induced spectral change in the charge-transfer band was studied. The results indicate that the spectral change is dependent on sample size and is wavelength selective. A detailed model was proposed to explain the light-induced spectral change.

Introduction

One-dimensional (1D) nanostructures, such as nanowires (NWs), nanorods, and nanotubes (NTs) have attracted extensive attention due to their unique physical and chemical properties.^{1–3} These systems, with two restricted dimensions, not only offer opportunities for investigating the dependence of electronic transport and optical and mechanical properties on size confinement and dimensionality^{4,5} but also play a crucial role in fields such as data storage⁶ and advanced catalyst and optoelectronic devices.^{2,7} Rare earth (RE) compounds were extensively applied to high-performance magnets, luminescence devices, catalysts, and other functional materials. Most of these functions depend strongly on the composition and structure of materials. Recently, the synthesis and spectroscopic properties of RE ion doped 1D devices have attracted considerable interest.^{8–14} Meyssamy et al. synthesized RE ion (RE = Tb^{3+} , Ce^{3+}) doped LaPO_4 NWs for the first time and reported their luminescent properties.¹⁰ Yada and Wang et al.^{11,14} reported the synthesis of RE hydroxide and oxide NWs. In some 1D nanomaterials, the luminescent properties of RE ions are modified in comparison to zero-dimensional nanoparticles (NPs) and traditional micrometer-sized powders, the so-called bulk materials. In one of our previous papers, we observed that the luminescent quantum efficiency of $^5\text{D}_1$ – $^7\text{F}_1$ transitions of Eu^{3+} in LaPO_4 NWs was enhanced more considerably than that of the corresponding NPs and the bulk powders.⁸ As the main and unsurpassed red

emitting materials in fluorescent lamps and projection television tubes, $\text{Y}_2\text{O}_3/\text{Eu}^{3+}$ phosphors inevitably gather more attention. Therefore, a lot of work has been performed on the luminescent properties of $\text{Y}_2\text{O}_3/\text{Eu}^{3+}$ zero-dimensional NPs during the past few years.^{15–19} In ref 12, the luminescent properties of 1D $\text{Y}_2\text{O}_3/\text{Eu}^{3+}$ NTs prepared by the surfactant assembly method were also reported, in which different symmetry sites of Eu^{3+} ions were observed. The spectroscopic properties in that paper have suggested that the structure of the $\text{Y}_2\text{O}_3/\text{Eu}^{3+}$ NTs is not pure cubic phase. It should be noted that the luminescent properties of RE ions strongly depend on crystal structure and preparation technique. Here, we have synthesized pure cubic phase $\text{Y}_2\text{O}_3/\text{Eu}^{3+}$ NTs as well as NWs by a hydrothermal method, which is similar to the preparation method reported by Wang et al.¹⁴ The luminescent properties of $\text{Y}_2\text{O}_3/\text{Eu}^{3+}$ NTs and NWs prepared by the hydrothermal method have not been studied yet. In this paper, their luminescent properties including electronic transition processes, local environments surrounding Eu^{3+} ions, electron–phonon coupling, and UV light irradiation induced spectral changes have been systematically investigated and compared.

Experiments

A. Sample Preparation. The $\text{Y}_2\text{O}_3/\text{Eu}^{3+}$ NTs and NWs were prepared by hydrothermal technique. Appropriate amounts of high-purity Y_2O_3 and Eu_2O_3 (1/0.01 mol ratio) were dissolved in concentrated HNO_3 first. Then the final pH value was adjusted to 12–13 with NaOH solution (0.2 M). After being stirred for 1 h, a milky colloid solution was transferred into several closed Teflon-lined autoclaves and subsequently heated at 130, 170, and 180 °C for 12 h, respectively. The obtained suspension was cooled to room temperature and was centrifuged at 2770g for

* To whom correspondence should be addressed. E-mail: hwsong2005@yahoo.com.cn. Fax: 86-431-6176320.

[†] Key Laboratory of Excited State Physics.

[‡] Graduate School of Chinese Academy of Sciences.

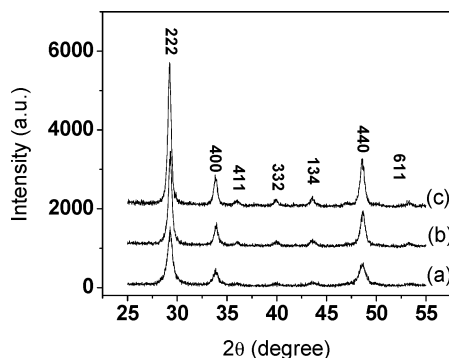


Figure 1. XRD patterns of Y₂O₃/Eu³⁺ powders prepared at different hydrothermal temperatures: (a) 130 °C, (b) 170 °C, (c) 180 °C.

20 min. The colorless supernatant including byproducts was discarded, washed with deionized water several times, and then dried at 70 °C. Finally, the obtained Y(OH)₃ powders were converted into Y₂O₃ by annealing at 500 °C for 2 h.

B. Measurements. X-ray diffraction (XRD) data were collected on a Rigaku D/max-rA X-ray diffractometer using a Cu target radiation source. Transmission electron micrographs (TEMs) and scanning electron micrographs (SEMs) were taken on JEM-2010 and JSM-5500 electron microscopes. Fluorescence and excitation spectra were recorded at room temperature using a Hitachi F-4500 spectrophotometer equipped with a continuous 150-W Xe-arc lamp. For comparison of different samples, the emission spectra were measured at a fixed bandpass of 0.2 nm with the same instrument parameters (2.5 nm for the excitation slit, 2.5 nm for the emission slit, and 700 V for the PMT voltage). In the experiments of spectral change induced by UV light irradiation, the monochromatic light separated from the same Xe-arc lamp was used as the irradiation source, which was with a slit of 10 nm. In the measurements of high-resolution emission spectra and fluorescence dynamics, a 266-nm laser generated from a pulsed Nd:YAG (aluminum garnet) laser combined with a fourth harmonic generator was used as a pump. It has a line width of 0.2 cm⁻¹, pulse duration of 10 ns, and repetition frequency of 10 Hz. A Rhodamine 6 G dye pumped by the same Nd:YAG laser was used as the frequency-selective excitation source. In the low-temperature experiments (77 K), the samples were put into a liquid nitrogen system. A Spex 1403 spectrometer, a photon-multiplier, and a boxcar integrator were used to record the high-resolution emission spectra and fluorescence dynamics.

Results and Discussion

A. Crystal Structure and Morphology. Figure 1 shows the XRD patterns of Y₂O₃/Eu³⁺ powders prepared at different hydrothermal temperatures. It can be seen that the crystal structures of all three samples belong to the pure cubic phase. No additional phase formed. The lower the hydrothermal temperature is, the broader the width of the XRD patterns. This indicates that the crystallite size of Y₂O₃/Eu³⁺ decreases at lower hydrothermal temperature.¹⁴

Figure 2 shows TEM or SEM images of nanosized Y₂O₃/Eu³⁺ prepared at different temperatures. It is obvious that the shapes of Y₂O₃/Eu³⁺ samples vary with preparation temperature. As shown in Figure 2a, the central part of the cylindrical sample prepared at 130 °C is white and the two peripheries are black, suggesting a tubular morphology. The products predominantly consist of nanotubes with outer diameters of 20–40 nm and length of ~1 μm. An individual tube shown in Figure 2b demonstrates that the tip of the tube is open, and the wall is

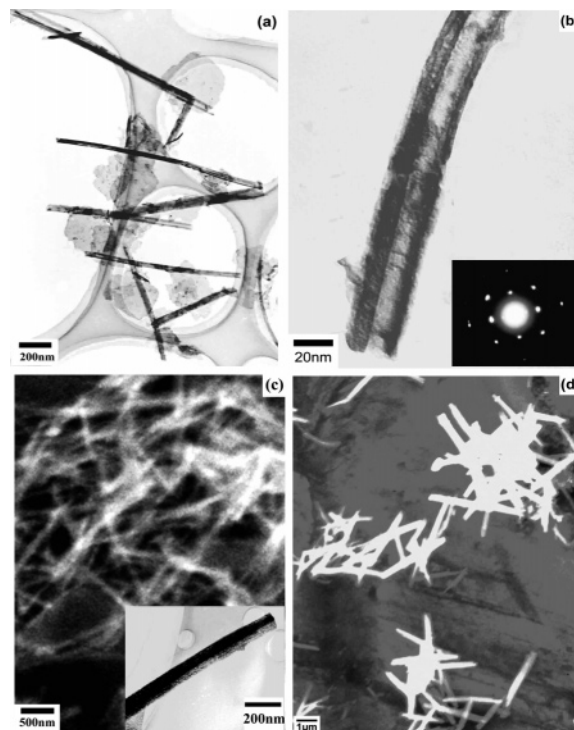


Figure 2. (a) TEM image of the Y₂O₃/Eu³⁺ sample prepared at 130 °C (NTs). (b) TEM image of an individual Y₂O₃/Eu³⁺ NT, inset of b electron diffraction patterns of the NT. (c) SEM image of the sample prepared at 170 °C (NW1), inset of c TEM image of an individual Y₂O₃/Eu³⁺ NW1. (d) SEM image of the sample prepared at 180 °C (NW2).

5–10 nm in thickness. So small size will lead to the broadening of XRD patterns; this is consistent with the result of the XRD experiment as shown in Figure 1. The other tubes have a similar thickness of wall. The inset of Figure 2b shows the electron diffraction pattern taken from a single nanotube, revealing its single-crystalline nature. As shown in parts c and d of Figure 2, the Y₂O₃/Eu³⁺ samples prepared at 170 and 180 °C both yield NWs. The inset of Figure 2c shows a TEM image of an individual NW. The NWs prepared at 170 °C have diameters of ~100 nm, while those prepared at 180 °C have diameters of ~300 nm. The lengths of the NWs prepared at different temperatures are 1–2 μm. In this article, the Y₂O₃/Eu³⁺ samples prepared at 130, 170, and 180 °C according to their shapes are named as NTs, NW1, and NW2, respectively.

B. Excitation and Emission Spectra. Figure 3 shows the excitation spectra of various Y₂O₃/Eu³⁺ NCs at room temperature. In Figure 3a, the broad band extending from 200 to 300 nm is assigned to the charge transfer (CT) transitions of Eu³⁺. The CTB of Y₂O₃/Eu³⁺ corresponds to the electronic transition from the 2p orbital of O²⁻ to the 4f orbital of Eu³⁺ and is related closely to the covalency between O²⁻ and Eu³⁺ and the coordination environment around Eu³⁺.²⁰ The CTB red shifts represent the increase in the covalency and the decrease in ionicity between oxygen and Eu³⁺.^{18,21} The sharp lines in Figure 3a are associated with the direct excitation of the f–f shell transitions of Eu³⁺. Their detailed origins have been labeled. It is seen that the intensity of the excitation spectra increases gradually with increasing sample diameter, while the intensity of the sharp lines relative to the band do not change. The maxima of the CTB hardly shift in different samples. This is different from the normal case in which the CTB has a shift when the sample size or dimension changes.^{16,22} No excitonic band below 220 nm was observed as the normal case in Y₂O₃/

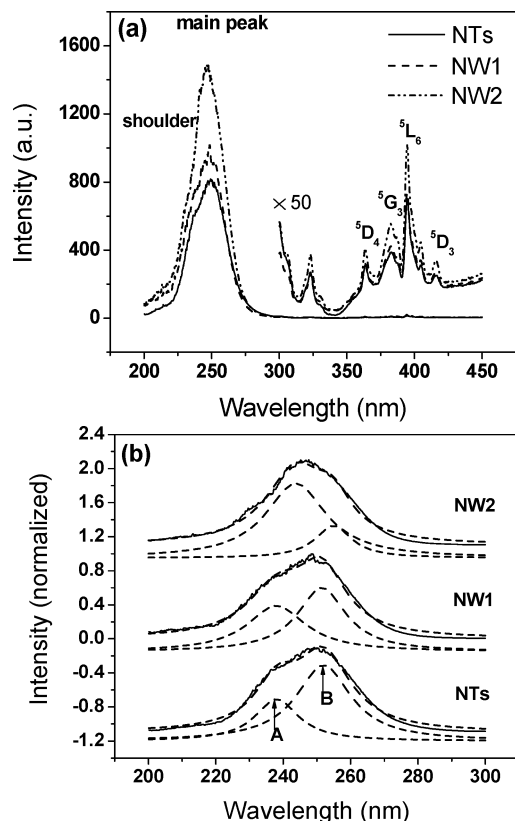


Figure 3. (a) Room-temperature excitation spectra of Eu^{3+} in different $\text{Y}_2\text{O}_3/\text{Eu}^{3+}$ powders ($\lambda_{\text{em}} = 611 \text{ nm}$). (b) decomposed CT bands by two Lorentzian functions.

Eu^{3+} nanoparticles.²³ It is interesting to observe that a shoulder appears in the short wavelength side of the main peak located at 246 nm. Hence, the CTB is decomposed into two Lorentzian components, A and B, as shown in Figure 3b. The ratio of component A to component B is determined to be 0.55 in the NTs, 0.71 in NW1, and 2.54 in NW2. It is apparent that from larger NWs to smaller NTs the relative intensity of component A to B becomes weak. This could be attributed to the variation of coordination environments around Eu^{3+} ions in three samples. In NCs, due to surface effects, such as surface adsorption, existence of surface dangling bonds, involvement of surface defects,²⁴ etc., the coordination environments around the surface Eu^{3+} ions should differ from that around the inner Eu^{3+} ions. As a consequence, the CT transitions of Eu^{3+} ions between the surface and the inner shift. In the three samples, the ratio of surface to volume varies, leading to the increase in CT transitions contributed by surface Eu^{3+} ions and the decrease in those contributed by the internal Eu^{3+} ions.

Figure 4 shows the emission spectra of $\text{Y}_2\text{O}_3/\text{Eu}^{3+}$ under the excitation of a 246-nm continuous light. The green emissions of $^5\text{D}_1-^7\text{F}_1$ (the emission of $^5\text{D}_1-^7\text{F}_1$ is dominant compared to other emissions of $^5\text{D}_1$ which are too weak to detect) and the red $^5\text{D}_0-^7\text{F}_J$ ($J = 0, 1, 2, 3$) transitions were observed, as labeled in the figure. Among these lines, the $^5\text{D}_0-^7\text{F}_2$ line is dominant in comparison to any other lines. The peak locations, the intensity ratio of $^5\text{D}_1-^7\text{F}_1$ to $^5\text{D}_0-\Sigma^7\text{F}_J$, and the ratio of $^5\text{D}_0-^7\text{F}_1$ to $^5\text{D}_0-^7\text{F}_2$ have hardly changed in different samples. The intensity ratio of $^5\text{D}_1-\Sigma^7\text{F}_J$ to $^5\text{D}_0-\Sigma^7\text{F}_J$ depends strongly on the nonradiative relaxation process of $^5\text{D}_1-^5\text{D}_0$. If the nonradiative transition rate of $^5\text{D}_1-^5\text{D}_0$ is faster than the radiative transition rate of $^5\text{D}_1-\Sigma^7\text{F}_J$, then the intensity of $^5\text{D}_1-\Sigma^7\text{F}_J$ is expected to decrease and can even disappear completely. The

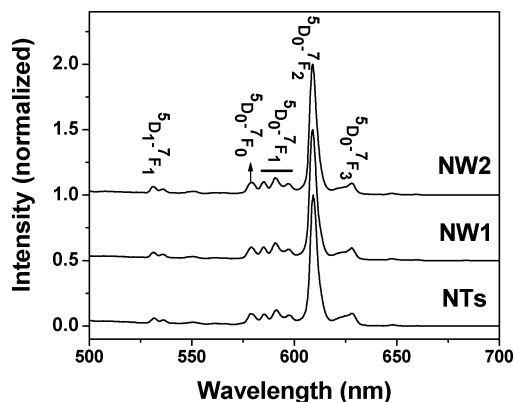


Figure 4. Room-temperature emission spectra of $\text{Y}_2\text{O}_3/\text{Eu}^{3+}$ under 246-nm excitation.

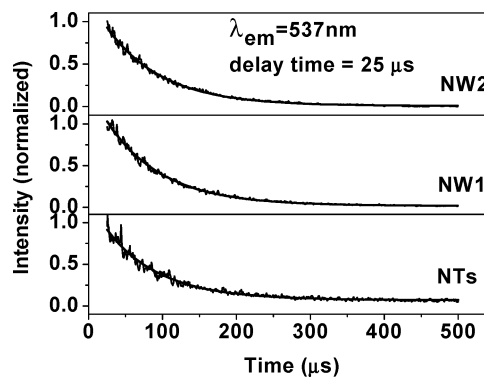


Figure 5. Fluorescence decay curves of the $^5\text{D}_1-^7\text{F}_1$ transitions at 537 nm under the 266-nm excitation at room temperature.

ratio of $^5\text{D}_0-^7\text{F}_2$ to $^5\text{D}_0-^7\text{F}_1$ is closely related to the local environments of Eu^{3+} .¹² Generally, the larger the intensity ratio of $^5\text{D}_0-^7\text{F}_2$ to $^5\text{D}_0-^7\text{F}_1$ is, the lower the local symmetry.²² The above results suggest that the nonradiative transition rate of $^5\text{D}_1-^5\text{D}_0$ is nearly the same, and the local environments of Eu^{3+} are similar in different samples. We suggest that the surface defect states involving NCs are located in the band gap of the Y_2O_3 host and are close to the conduction band, which is much higher than the $^5\text{D}_J$ states of Eu^{3+} ions. In this case, the surface defects do not contribute to the nonradiative relaxation among the lower $^5\text{D}_J$ states. Therefore, the nonradiative relaxation rate of $^5\text{D}_1-^5\text{D}_0$ in different samples hardly changes.

C. Luminescent Dynamics. Figure 5 shows the fluorescence decay curves of the $^5\text{D}_1-^7\text{F}_1$ transitions measured when the delay time (“delay time” means the internal time lasting from the time when excitation pulse is terminated to the time the fluorescence start to detected) is 25 μs . As can be seen, the $^5\text{D}_1-^7\text{F}_1$ transitions decayed exponentially. By fitting, the fluorescence lifetimes of $^5\text{D}_1-^7\text{F}_1$ in different samples were determined to be 68.2 μs in NTs, 75.2 μs in NW1, and 75.2 μs in NW2. This indicates that the total electronic transition rate of the $^5\text{D}_1$ level including the radiative transition rate of $^5\text{D}_1-^7\text{F}_1$ and the nonradiative relaxation rate of $^5\text{D}_1-^5\text{D}_0$ in NTs has only a little variation in comparison to that in the NWs. As discussed in the above section, the nonradiative relaxation rate of $^5\text{D}_1-^5\text{D}_0$ in different samples hardly changes; thus it can be concluded that the luminescent quantum efficiency of $^5\text{D}_1$ in different samples has little variation.

Figure 6a shows the fluorescence decay curves of the $^5\text{D}_0-^7\text{F}_2$ transitions measured when delay time is 0.5 ms, which is much longer than the lifetime of $^5\text{D}_1$. It can be seen that as the delay time is longer, the emissions of $^5\text{D}_0-^7\text{F}_2$ decay exponen-

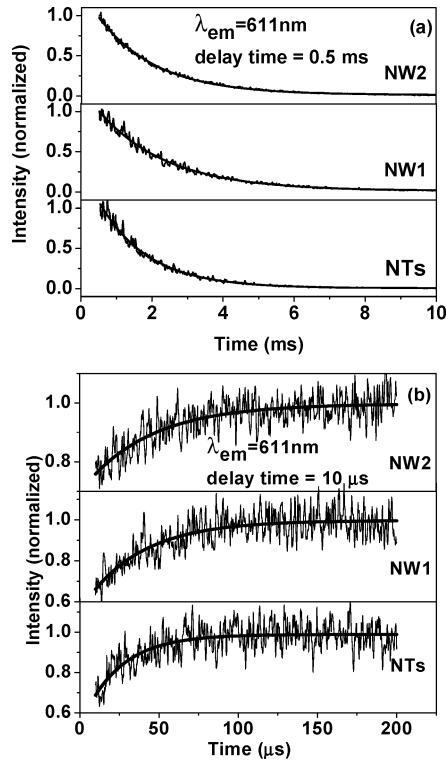


Figure 6. Fluorescence decay curves of the $^5D_0-^7F_2$ transitions at 611 nm: (a) measured when delay time is 0.5 ms, (b) measured when delay time is 10 μ s.

tially for all samples. The lifetime of the 5D_0 state was determined to be 1.36 ms in NTs, 1.91 ms in NW1, and 1.65 ms in NW2. The fluorescence lifetime equals the inverse of the total radiative and nonradiative transition rates. Generally, the energy gap between 5D_0 and the nearest excited state 7F_6 is as high as 12 000 cm^{-1} , which is much larger than any phonon energy in the Y₂O₃ host. In this case, nonradiative relaxation hardly happens according to the theory of multiphonon relaxation.^{22,24} However, some works reported that adsorbates on the surface may have higher vibration frequencies, especially O–H vibration, and these may lead to higher multiphonon emission in nanocrystalline samples.²⁴ Actually, we measured the lifetime of 5D_0 from 10 to 300 K, which hardly changed in the three samples. Thus, we suggest that lifetime of 5D_0 is dominated by the radiative transition rate of $^5D_0-\Sigma^7F_J$. In the NTs, the radiative transition rate should be a little larger than that in the NWs.

Figure 6b shows the fluorescence decay curves of the $^5D_0-^7F_2$ transitions measured when the delay time is 10 μ s. As the delay time becomes shorter, the fluorescent intensity increases initially, then approaches a maximum, and then decays slowly. Under 266-nm excitation, electrons from ground states are pumped to CT states first, and then nonradiatively relax to the excited state 5D_J . Two paths exist for populating the 5D_0 level, the CT feeding, and the $^5D_1-^5D_0$ relaxation. The transitions from CT states to Eu³⁺ ions are very fast. The rise process in the time scale of several tens of microseconds should be induced by the nonradiative relaxation of $^5D_1-^5D_0$. Considering the nonradiative relaxation of $^5D_1-^5D_0$, the electron population of 5D_0 and 5D_1 as a function of time can be derived as

$$N_0(t) = N_0(0)e^{-R_0 t} + N_1(0) \frac{W_{10}}{R_1 + W_{10} - R_0} \times (e^{-R_0 t} - e^{-(R_1 + W_{10})t}) \quad (1)$$

$$N_1(t) = N_1(0)e^{-(W_{10} + R_1)t} \quad (2)$$

(see Supporting Information) where $N_0(t)$ or $N_1(t)$ represents the electron population of 5D_0 or 5D_1 at a certain time t , $N_0(0)$ or $N_1(0)$ represents the electron population of 5D_0 or 5D_1 immediately after one excitation pulse terminates ($t = 0$), R_0 or R_1 represents the total radiative transition rate of $^5D_0-\Sigma^7F_J$ or $^5D_1-\Sigma^7F_J$, and W_{10} represents the nonradiative relaxation rate of $^5D_1-^5D_0$. According to eq 1 and assuming $R_1 \gg R_0$, the electron population of 5D_0 as a function of time can be written as

$$N_0(t) = I_0 \exp(-t/\tau_0) - I_1 \exp(-t/\tau_1) \quad (3)$$

with $\tau_0 = 1/R_0$, $\tau_1 = 1/(R_1 + W_{10})$, $I_0 \propto N_0(0) + N_1(0)[1 - QE_1]$, and $I_1 \propto N_1(0)[1 - QE_1]$. Here, $QE_1 = R_1/(R_1 + W_{10})$ is the luminescent quantum efficiency of 5D_1 . According to eq 3 and the values of the lifetimes of 5D_1 and 5D_0 , the luminescent dynamics in Figure 6b were well fitted. By fitting, I_0/I_1 was determined to be 2.5 in NTs, 2.3 in NW1, and 2.7 in NW2. In light of eq 3, the electron population ratio of 5D_1 to 5D_0 at $t = 0$ can be expressed as

$$N_0(0)/N_1(0) = (I_0/I_1 - 1)(1 - QE_1) \quad (4)$$

Under continuous excitation, the rate equation at steady state can be written as

$$R_{CT0}N_C - R_0N_0' + W_{10}N_1' = 0 \quad (5)$$

$$R_{CT1}N_C - (W_{10} + R_1)N_1' = 0 \quad (6)$$

where N_C is the number of O²⁻ being excited, R_{CT0} or R_{CT1} is the CT rate from excited-state O²⁻ to the 5D_0 or 5D_1 level of Eu³⁺, and N_0' or N_1' is the electron population of 5D_0 or 5D_1 at the steady state. According to the definition of $N_1(0)$ and $N_0(0)$, $R_{CT0}/R_{CT1} = N_0(0)/N_1(0)$ is valid. In light of eqs 5 and 6, we have

$$\frac{N_1'}{N_0'} = \frac{R_0}{(W_{10} + R_1) \frac{N_0(0)}{N_1(0)} + W_{10}} \quad (7)$$

The intensity ratio of $^5D_1-\Sigma^7F_J$ to $^5D_0-\Sigma^7F_J$ can be expressed as

$$\alpha = \frac{I_1'}{I_0'} = \frac{R_1 N_1'}{R_0 N_0'} \quad (8)$$

where I_0' and I_1' represent the steady-state emission intensity of $^5D_0-\Sigma^7F_J$ and $^5D_1-\Sigma^7F_J$, respectively. On the basis of eqs 7 and 8, we have

$$N_0(0)/N_1(0) = \left(\frac{1}{\alpha} + 1\right)QE_1 - 1 \quad (9)$$

$1/\alpha$ can be determined from the emission spectra under continuous excitation shown in Figure 4 to be 7.14 in NTs, 6.87 in NW1, and 7.48 in NW2. Combining eqs 4 and 9, QE_1 was determined to be 25.9% in NTs, 25.1% in NW1, and 26.5% in NW2, and $N_0(0)/N_1(0)$ was determined to be 1.11 in NTs, 0.97 in NW1, and 1.25 in NW2. It is apparent that the numerical values of $N_0(0)$ and $N_1(0)$ are nearly same. The electron populations in the 5D_0 state come from both the nonradiative CT and the $^5D_1-^5D_0$ relaxation.

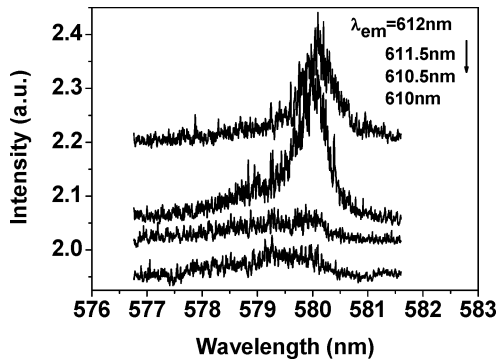


Figure 7. 7F_0 – 5D_0 excitation spectra of NW1 monitoring different emission wavelengths of the 5D_0 – 7F_2 transitions at 77 K in NW1.

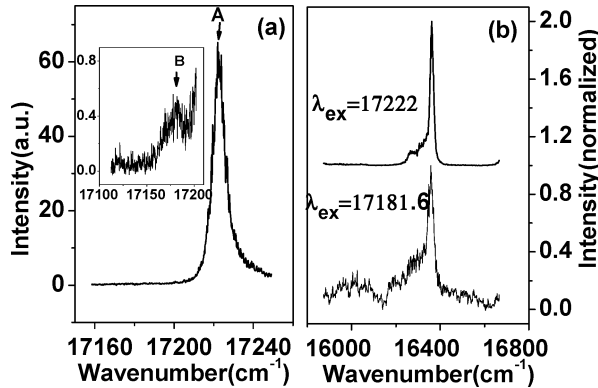


Figure 8. (a) Excitation spectrum of 7F_0 – 5D_0 ($\lambda_{em} = 611$ nm), inset, the wing peak appeared at the low energy side of the main peak. (b) Emission spectra of 5D_0 – 7F_2 under the excitation of different wavelengths. The above experiments are all performed in Y_2O_3/Eu^{3+} NTs at 77 K.

C. Phonon Sidebands and Electron–Phonon Coupling.

The frequency-selective excitation experiments at 77 K were performed to reveal the symmetry site of Eu^{3+} in the Y_2O_3/Eu^{3+} NTs and NWs. The energy level of Eu^{3+} at different symmetry sites should have some variation due to the crystal-field effect. By frequency-selective excitation, the luminescence contributed by Eu^{3+} at different sites can be distinguished if it exists. Figure 7 shows the 7F_0 – 5D_0 excitation spectra obtained by monitoring different locations of the 5D_0 – 7F_2 transitions in NW1. It can be seen that as different wavelengths are monitored, only one 7F_0 – 5D_0 excitation peak appears, at 580.1 nm (17 238 cm^{-1}). The 5D_0 and 7F_0 states do not split in the crystal field; therefore, the 5D_0 – 7F_0 transition is commonly utilized to deduce the number of symmetry sites. One excitation peak corresponds to one symmetry site. Therefore, we can conclude that in the pure cubic phase, Y_2O_3/Eu^{3+} NTs/NWs prepared by the present hydrothermal method, only one C_2 symmetry site of Eu^{3+} appears in the emissions of 7F_0 – 5D_0 , as reported in the bulk. Actually, Eu^{3+} ions occupy two symmetry sites in the Y_2O_3 host, C_2 (75%) and S_6 (25%). Generally, the electronic dipole transition of Eu^{3+} ions at the C_2 site is partially allowed, while the electronic dipole transition at the S_6 site is forbidden.²⁵ It should be noted that in cubic Y_2O_3/Eu^{3+} NPs prepared by combustion, we observed an extra broader excitation peak at 579.9 nm (17 244 cm^{-1}) besides the 580.6 nm (17 222 cm^{-1}) line, which was attributed to the emission of Eu^{3+} at the disordered surface site. In the present, well-crystallized, Y_2O_3 single crystal, no extra excitation peak caused by amorphous phase is observed.

Figure 8a shows the 7F_0 – 5D_0 excitation spectrum monitoring the emission of 5D_0 – 7F_2 in Y_2O_3/Eu^{3+} NTs. Besides the main

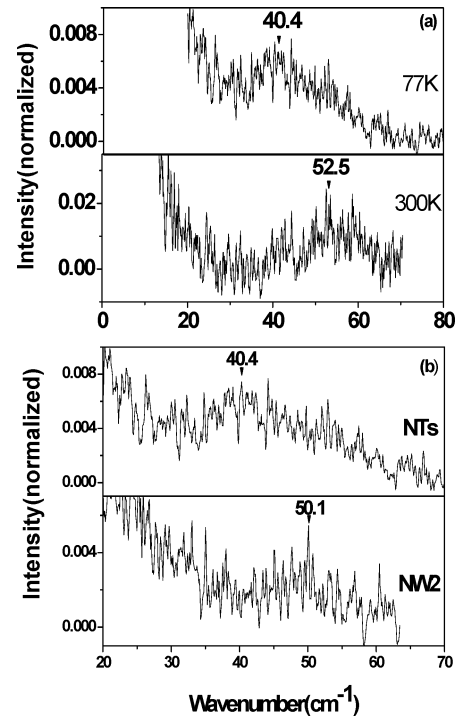


Figure 9. Position of phonon sideline spectra related to the 7F_0 – 5D_0 zero phonon transitions: (a) at two different temperatures in NTs and (b) in different samples at 77 K.

peak (marked as A) at 17 222 cm^{-1} , the other wing peak (marked as B) appears in the low-energy side, which is 2 orders of magnitude weaker than the main peak. Figure 8b demonstrates a comparison of the 5D_0 – 7F_2 emissions excited at different locations, the wing (17 181.6 cm^{-1}) and the main peak (17 222 cm^{-1}). The spectral configurations excited at different locations are nearly the same, indicating that the wing and the main peak come from the same symmetry site. Peak B can be attributed to the phonon sideline of peak A. This is further confirmed by the excitation spectra at various temperatures, as shown in Figure 9a. As can be seen, the intensity of peak B obviously increases, and the position related to peak A shifts to the high-energy side as the temperature varies from 77 to 300 K. This is a feature of the phonon sideline, instead of different symmetry sites.²⁵ The intensity of the phonon sideline related to the zero phonon line can be written approximately as²⁶

$$\frac{I(\omega)}{I_0} = \frac{\left| \sum_j \alpha_{j,\omega} \langle l | d | j \rangle + \sum_j \beta_{j,\omega} \langle j | d | i \rangle \right|^2 \rho(\omega, T)}{|\langle l | d | i \rangle|^2} \quad (10)$$

with

$$\alpha_{j,\omega} = \sqrt{\frac{\hbar}{2\omega}} \frac{\left\langle j \left| \partial \frac{H_{el}}{\partial q_\omega} \right| i \right\rangle \langle n+1 | a_\omega^\dagger | n \rangle}{E_i - E_j - \hbar\omega} \quad (11)$$

$$\beta_{j,\omega} = \sqrt{\frac{\hbar}{2\omega}} \frac{\left\langle j \left| \partial \frac{H_{el}}{\partial q_\omega} \right| i \right\rangle \langle n-1 | a_\omega | n \rangle}{E_i - E_j + \hbar\omega} \quad (12)$$

where $I(\omega)$ is the intensity of the phonon sideline at frequency ω , I_0 is the intensity of the zero phonon line, H_{el} is the operator energy of electron–phonon coupling, q_ω is the normal-mode

coordinate, E_i and E_j are the energies of the eigenstates $|i\rangle$ and $|j\rangle$, respectively, d is the operator transition, $|i\rangle$ is initial state of electron, $|l\rangle$ is final state of electron, $|j\rangle$ is the eigenstate of electron, and $\rho(\omega, T)$ is the phonon density, which strongly depends on frequency and temperature

$$\rho(\hbar\omega, T) = \frac{1}{\exp(\hbar\omega/kT) - 1} \quad (13)$$

where $\hbar\omega$ is the phonon energy and k is Boltzmann's constant. On the basis of eqs 10 and 13, the density at the state ω of the phonon decreases with decreasing temperature in which the density of the phonon at the lower energy state is larger, so the red shift occurs at 77 K compared to 300 K. At the same time, the intensity of the phonon sideline becomes stronger.²⁷

A comparison of phonon sidelines in different Y₂O₃/Eu³⁺ powders was drawn as Figure 9b. As the powders varied from NW2 to NTs, the relative intensity of the phonon sideband increased and shifted red, indicating stronger electron–phonon coupling. From the theoretical results of Tamura et al.,²⁸ the modes of the phonons can be classified into two types: the inner modes having high eigenfrequencies and the surface modes having low eigenfrequencies. The surface-to-volume ratio of the Y₂O₃/Eu³⁺ NTs increases more rapidly than that of NW2; thus the surface modes (low eigenfrequencies) make more contributions to the phonon sideline, leading to the red shift of the phonon sideline. It should be noted that we have not found any literature on the phonon sideline of Y₂O₃/Eu³⁺ NPs. The electron–phonon coupling has a close relationship with the modes of electrons and phonons. As is well-known for f-electron states of rare earth ions, the diameter of the electronic wave function is of the order of 10⁻¹ nm, which is much smaller than the sample diameter. The size confinement effect does not work. For the wave function of a long acoustic wave, the size confinement effect is valid: The acoustic phonon modes become discrete, and the confinement of the vibration excitations produces a greatly enhanced interaction between the ion electron states and the vibrational modes.²⁹ We consider that shape anisotropy may influence low-energy acoustic vibrational modes, and the modes along the longitudinal direction of the one-dimensional materials may be different from that in nanoparticles. The phonon sideline observed in Y₂O₃/Eu³⁺ NTs and NWs is likely from coupling between longitudinal phonon modes and electronic modes.

D. Fluorescence Change before and after Light Irradiation. Figure 10a shows the CTB before and after UV light irradiations with different wavelengths for 20 min in Y₂O₃/Eu³⁺ NTs. As can be seen, the intensity in the CTB decreases as a whole as the sample is irradiated with a 230- or 245-nm light. As the sample is irradiated with a 260-nm light, the intensity at the longer wavelength side of the CTB has a small decrease, while that at the shorter wavelength side increases by a larger amount. This demonstrates that the UV irradiation induced spectral change is wavelength selective. The excited CTBs before and after UV light irradiation were decomposed into two components also, as shown in Figure 10b. Figure 10b more obviously demonstrates that as the sample is irradiated with 230- or 246-nm light, the intensity in peak B decreases considerably, while that in peak A has only a small decrease. As the sample is irradiated with 260-nm light, the component of peak B decreases, while the component of peak A increases. The intensity variation in CTB under UV exposure depends strongly on the sample diameter. Figure 11 shows the dependence of normalized emission intensity at 611 nm on time in different samples exposed to the same conditions. It is apparent that the

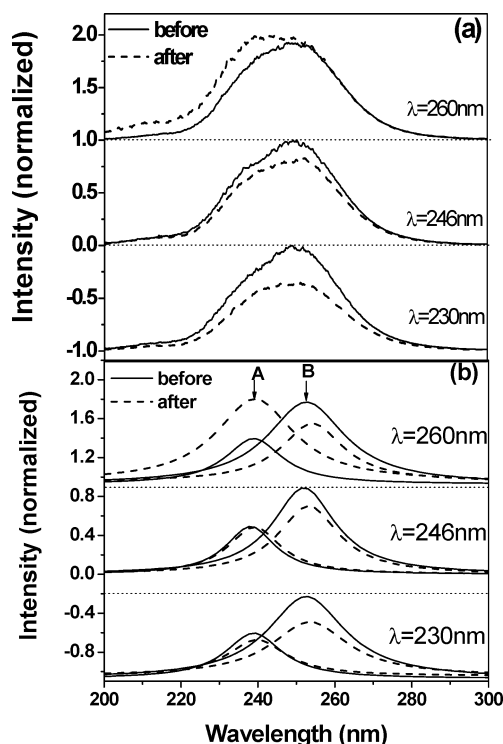


Figure 10. (a) Excited CT bands Eu³⁺ in Y₂O₃ NTs ($\lambda_{\text{em}} = 611$ nm) measured before and after irradiation with various lights. (b) Decomposed spectra.

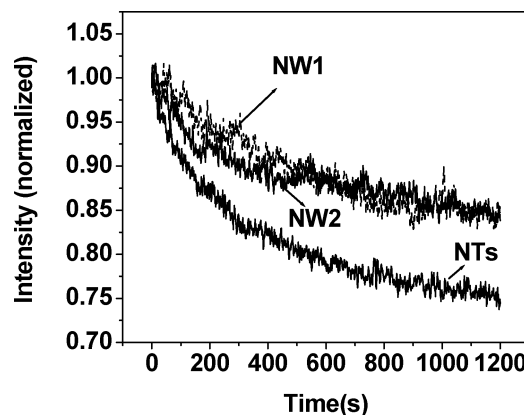


Figure 11. Dependence of normalized intensity at 611 nm on irradiation time of 230-nm light in different samples.

relative change in NTs is much larger than that in NW1 and NW2. In one of our previous papers, we have studied the UV light irradiation induced spectral change in cubic Y₂O₃/Eu³⁺ NPs prepared by combustion.¹⁸ The present results are similar to that in Y₂O₃/Eu³⁺ NPs.¹⁸ Through irradiation by weaker UV light, the light-induced spectral change in Y₂O₃/Eu³⁺ NCs can be attributed to the local environment change surrounding Eu³⁺ ions, instead of the photoreduction from Eu³⁺ to Eu²⁺.¹⁸ The evidence is that the f–f shell transition lines do not change upon UV exposure. The variation of CTB exposure with UV light is related to surface effects. The local environments for the Eu³⁺ ions in/near the surface are easily rearranged by UV irradiation, because of the existence of numerous surface defects, leading to a change in the CTB.¹⁸

We consider that different processes exist which contributed to the change in CTB under UV irradiation. One process is that some of the electrons on the 2p excited states of O²⁻ are captured by the nearby defects through tunneling. This process is against the CT transition from O²⁻ to Eu³⁺, thus leading the

intensity in CTB to decrease. The change in CTB under the exposure at 230 and 246 nm is in agreement with this process. The other process is that the relative disordered local environment surrounding surface Eu^{3+} ions becomes relative order, leading to the decrease of the relative-disordered component B and the increase of the relative-ordered component A. During this process, the surface defects such as oxygen vacancies are modified as well, leading to the enhancement of photoluminescence.³⁰ Surface defects generally act as nonradiative transition channels, causing the quenching of photoluminescence. The change in CTB under exposure at 260 nm is well in accordance with the description of this process.

Conclusions

1D pure cubic nanosized $\text{Y}_2\text{O}_3/\text{Eu}^{3+}$ powders were synthesized by the hydrothermal method at different temperatures. The shape and size vary strongly with hydrothermal temperature. The powders prepared at 130 °C yield NTs, with wall thickness of 5–10 nm and outer diameter of 20–40 nm. The powders prepared at 170 and 180 °C yield NWs, with diameters of ~100 and ~300 nm, respectively. The lengths of all the powders are 1–2 μm .

The results of excitation spectra demonstrate that the configuration of the excited CTB of Eu^{3+} varies with sample diameter and is decomposed into the contribution of two components. This is attributed to the variation of coordination environments around Eu^{3+} ions in three samples.

The fluorescence lifetime of $^5\text{D}_1\text{--}^7\text{F}_1$ has little variation in different samples, while that of $^5\text{D}_0\text{--}^7\text{F}_2$ decreases a little in $\text{Y}_2\text{O}_3/\text{Eu}^{3+}$ NTs. The rise process with a time of several tens of microseconds was observed in the fluorescence dynamics of $^5\text{D}_0$, corresponding to the decay time of $^5\text{D}_1$.

The frequency-selective excitation experiment was performed in different samples. The result indicates that in $\text{Y}_2\text{O}_3/\text{Eu}^{3+}$ NTs and NWs the photoluminescence of the $^5\text{D}_0\text{--}^7\text{F}_1$ transitions originate from Eu^{3+} ions at one symmetry site (C_2), like that in the bulk. The phonon sideline is observed at the low-energy side of the $^7\text{F}_0\text{--}^5\text{D}_0$ zero phonon line. The relative intensity of the sideline to the zero phonon line increases with elevated temperature and the increased diameter of sample. The location shifts blue with elevated temperature and decreased diameter.

The UV light irradiation induced spectral change in CTB was studied. The results indicate that the spectral change is dependent on sample size and is wavelength selective. The smaller the sample size is, the larger the light-induced change. Under 230- and 246-nm irradiation, the CTB decreases as a whole. Under 260-nm irradiation, the CTB at the long wavelength side decreases, while that at the short wavelength side increases. This change is attributed to the rearrangements of local environments surrounding Eu^{3+} ions. A detailed model is proposed to explain the light-induced spectral change of CTB.

Acknowledgment. The authors thank National Natural Science Foundation of China (Grant 10374086) and Talent Youth Foundation of JiLin Province (Grant 20040105) for their financial support.

Supporting Information Available: Rate equations governing the level of the population of two states, $^5\text{D}_1$ and $^5\text{D}_0$, and equations of the time dependence of their population numbers, $N_1(t)$ and $N_0(t)$. This material is available free of charge via the Internet at <http://pubs.acs.org>.

References and Notes

- (1) Iijima, S. *Nature (London)* **1991**, 354, 56.
- (2) Wang, X. F.; Lieber, C. M. *Nature (London)* **2001**, 409, 66.
- (3) Dickey, E. C.; Crimes, C. A.; Jain, M. K.; Ong, K. G.; Qian, D.; Kichambare, P. D.; Andrews, R.; Jacques, D. *Appl. Phys. Lett.* **2001**, 79, 4022.
- (4) Huang, M.; Mao, S.; Feick, H.; Yan, H.; Wu, Y.; Kind, H.; Weber, E.; Russo, R.; Yang, P. *Science* **2001**, 292, 1897.
- (5) Xia, Y.; Yang, P. *Adv. Mater.* **2003**, 15, 351.
- (6) Kong, Y. C.; Yu, D. P.; Zhang, B.; Fang, W.; Feng, S. Q. *Appl. Phys. Lett.* **2001**, 78, 4.
- (7) Kind, H.; Yan, H.; Law, M.; Messer, B.; Yang, P. *Adv. Mater.* **2002**, 14, 158.
- (8) Song, H.; Yu, L.; Lu, S.; Wang, T.; Liu, Z.; Yang, L. *Appl. Phys. Lett.* **2004**, 85, 470.
- (9) Yu, L.; Song, H.; Lu, S.; Liu, Z.; Yang, L. *Chem. Phys. Lett.* **2004**, 399, 384.
- (10) Meyssamy, H.; Riwotzki, K.; Kornowski, A.; Nased, S.; Haase, M. *Adv. Mater. (Weinheim, Ger.)* **1999**, 11, 840.
- (11) Yada, M.; Mihara, M.; Mouri, S.; Kijima, T. *Adv. Mater. (Weinheim, Ger.)* **2002**, 14, 309.
- (12) Wu, C.; Qin, W.; Qin, G.; Zhao, D.; Zhang, J.; Huang, S. *Appl. Phys. Lett.* **2003**, 82, 520.
- (13) Jia, C.; Sun, L.; Luo, F.; Jiang, X.; Wei, L.; Yan, C. *Appl. Phys. Lett.* **2004**, 84, 5305.
- (14) Wang, X.; Li, Y. *Chem.—Eur. J.* **2003**, 9, 5627.
- (15) Meltzer, R.; Feofilov, S.; Tissue, B.; Yuan, H. *Phys. Rev. B* **1999**, 60, 14012.
- (16) Qi, Z.; Shi, C.; Zhang, W.; Zhang, W.; Hu, T. *Appl. Phys. Lett.* **2002**, 81, 2857.
- (17) Igarashi, T.; Ihara, M.; Kusunoki, T.; Ohno, K.; Isobe, T.; Senna, M. *Appl. Phys. Lett.* **2000**, 76, 1549.
- (18) Song, H.; Chen, B.; Peng, H.; Zhang, J. *Appl. Phys. Lett.* **2002**, 81, 1776.
- (19) Peng, H.; Song, H.; Chen, B.; Wang, J.; Lu, S.; Kong, X.; Zhang, J. *J. Chem. Phys.* **2003**, 118, 1.
- (20) Hoefdraad, H. E. *J. Solid State Chem.* **1975**, 15, 175.
- (21) Wanmaker, W. L.; Bril, A.; Vrugt, J. W. T.; Broos, J. *Philips Res. Rep.* **1966**, 21, 270.
- (22) Yu, L.; Song, H.; Lu, S.; Liu, Z.; Yang, L.; Kong, X. *J. Phys. Chem. B* **2004**, 108, 16697.
- (23) Konrad, A.; Fries, T.; Gahn, A.; Kummer, F.; Herr, U.; Tidecks, R.; Samwer, K. *J. Appl. Phys.* **1999**, 86, 3129.
- (24) Schmechel, R.; Kennedy, M.; Seggern, H.; Winkler, H.; Kolbe, M.; Fischer, R.; Li, X.; Benker, A.; Winterr, M.; Hahn, H. *J. Appl. Phys.* **2001**, 89, 1679.
- (25) Peng, H.; Song, H.; Chen, B.; Lu, S.; Huang, S. *Chem. Phys. Lett.* **2003**, 370, 485.
- (26) Yu, J. *Physics of Luminescence*; Changchun Press: p 59.
- (27) Tanabe, S.; Todoroki, S.; Hirao, K.; Soga, J. *Non-Cryst. Solids* **1990**, 122, 59.
- (28) Tamura, A.; Ichinokawa, T. *J. Phys. C: Solid State Phys.* **1983**, 16, 4779.
- (29) Yang, H.; Hong, K. S.; Feofilov, S. P.; Tissue, B. M.; Meltzer, R. S.; Dennis, W. M. *J. Lumin.* **1999**, 83, 139.
- (30) Wang, J.; Song, H.; Sun, B.; Ren, X.; Chen, B.; Xu, W. *Chem. Phys. Lett.* **2003**, 379, 507.